ADVANCED OPTICAL MATERIALS
www.advopticalmat.de

Tailoring Plasmonics of Au@Ag Nanoparticles by Silica Encapsulation

Johannes Schultz, Felizitas Kirner, Pavel Potapov, Bernd Büchner, Axel Lubk, and Elena V. Sturm**

Hybrid metallic nanoparticles (NPs) encapsulated in oxide shells are currently intensely studied for plasmonic applications in sensing, medicine, catalysis, and photovoltaics. Here, a method for the synthesis of Au@Ag@SiO_2 cubes with a uniform silica shell of variable and adjustable thickness in the nanometer range is introduced and their excellent, highly reproducible, and tunable optical response is demonstrated. Varying the silica shell thickness, the excitation energies of the single NP plasmon modes can be tuned in a broad spectral range between 2.55 and 3.25 eV. Most importantly, a strong coherent coupling of the surface plasmons is revealed at the silver–silica interface with Mie resonances at the silica–vacuum interface leading to a significant field enhancement at the encapsulated NP surface in the range of 100% at shell thicknesses $t \simeq 20$ nm. Consequently, the synthesis method and the field enhancement open pathways to a widespread use of silver NPs in plasmonic applications including photonic crystals and may be transferred to other non-precious metals.

1. Introduction

Localized surface plasmon (LSP) resonances of (noble) metal nanoparticles (NPs) with a size comparable or smaller than the wavelength of incident light lead to intriguing optical properties such as frequency-dependent electromagnetic field confinement and amplification. These are exploited in a multitude of applications, such as sensors,[1] spectroscopy signal enhancement,[2] nanoantennas[3] and catalysis,[4] where the frequency of the surface plasmons on individual particles can be tuned specifically by varying compositions (e.g., use of different metals or alloys),[5,6] morphology and size of the particles,[7] and environment (e.g., different dielectric surroundings).[8] The latter offers a particular rich playground ranging from mere frequency tuning over generation of hybridized surface plasmon modes[9–11] and plasmon bands[5,12] in NP oligomers, polymers, and superlattices, to strong coherent coupling between surface plasmons and other excitations such as excitons.[8] Here, the NP morphology, their interparticle distance, and arrangement within the assembly define the coupling strength and hence the resonance energies of the coupled mode.[12–17]

Generally, the fabrication of plasmonic nanostructures may be categorized into top-down and bottom-up approaches. Electron-beam lithography[16,18,19] belongs to the latter and allows a precise control of dimension, geometry, and interparticle distance of the NPs. Zhu et al.,[18] for instance, present a method to lithographically produce pairs of silver particles with narrow 3 nm gaps. Notwithstanding, this pathway also faces several downsides concerning the crystal quality of lithographically fabricated (noble) metal nanostructures, control over 3D shape of NPs down to nanometer length scales[18,19] and fabrication of large NP arrangements in particular 3D photonic crystals.[20]

A bottom-up approach for the design of nanostructures that partially overcomes the aforementioned issues is the (self-) assembly of NPs. A particularly simple method is the drying of a dilute NP dispersion.[21] More sophisticated methods include DNA origami,[22,23] assembly by a gas-phase diffusion technique[24,25] or under weak external magnetic fields,[26] and self-assembly on patterned substrates.[12] The advantage of these methods lies in the high quality of the NPs and the straightforward upscaling of some of the self-assembly methods. Drawback is the reduced flexibility in deliberately arranging the NPs compared to lithographical methods, for example, the precise adjustment of interparticle distances[8] or the deliberate creation of NP superlattices (e.g., colloidal crystals, mesocrystals[27]). However, to purposefully influence the

J. Schultz, P. Potapov, B. Büchner, A. Lubk
Institute for Solid State Research
Leibniz Institute for Solid State and Materials Research Dresden
Helmholtzstraße 20, 01069 Dresden, Germany
E-mail: a.lubk@ifw-dresden.de

F. Kirner, E. V. Sturm
Department of Chemistry
University of Konstanz
Universitätsstraße 10, 78457 Konstanz, Germany
E-mail: elena.sturm@uni-konstanz.de

B. Büchner, A. Lubk
Institute of Solid State and Materials Physics
TU Dresden
Haeckelstraße 3, 01069 Dresden, Germany

The ORCID identification number(s) for the author(s) of this article can be found under https://doi.org/10.1002/adom.202101221.

DOI: 10.1002/adom.202101221

superlattice arrangement is out of the scope of this paper and needs additional elaboration.

Highly crystalline noble metal NPs with specific shapes and sizes can be synthesized by a variety of methods. One of the most prominent procedures for the synthesis of well-defined particles is the seed-mediated growth method.[28,29] Therein, nucleation and growth process are largely separated, which allows individual optimization of experimental parameters. NPs are thermodynamically unstable due to their high surface to volume ratio which is why most syntheses employ surfactants to stabilize the NPs and control their morphology.[30–33] Single crystalline gold NPs can be reproducibly synthesized in aqueous solution at mild reaction conditions.[34] Silver NPs may require more elaborate methods with harsher conditions and the reproducibility depends on several synthesis parameters.[35] Yet, gold-silver core–shell nanocubes can be produced at high yields using a seed-mediated synthesis with single crystalline gold particles as seeds and cetyltrimethylammonuim chloride (CTAC) as surfactant.[36] This epitaxial overgrowth of silver onto gold is a less elaborate process leading to a higher reproducibility compared to the synthesis of single crystalline silver NPs.

It is important to note that surfactants often deteriorate the plasmonic properties of metallic NPs by modifying the dielectric properties of the crucial metal-to-environment interfaces. After the assembly of NPs, remaining surfactants should be therefore removed from the particle surface, for example, by plasma cleaning. However, a complete or nearly complete removal of the stabilizer can lead to destabilization, shape-loss, and fusion of the NPs. In particular, unprotected silver NPs are quite sensitive to modification and deterioration. For instance, the oxidization of silver can cause distorted NPs with a silver-oxide shell of poor optical response. The shell's thickness is mostly unclear and changing.[8] In consequence, the plasmonic response of silver NPs deteriorates, shifts over time and is generally not-well defined.[5] This is one of the reasons why silver is a relatively unpopular plasmonic material, despite its broad plasmon band and low loss in the optical regime.

These stability issues can be circumvented with an encapsulation by silica (high optical transmittance in the optical frequency range) as shown by flame aerosol method for the synthesis of Au@Ag NPs followed by a swirl injection of silica precursor vapor.[37] For NPs in solution, a silica encapsulation is generally performed using a modified Stöber process[38,39] following the NP synthesis and removal of excess surfactants (e.g., CTAC). As a transfer of the NPs from aqueous solution to an ethanol–water mixture is necessary, the high surface potential of positively coated NPs needs to be screened first by polyelectrolytes or polymers to avoid aggregation.[40] As a result, after encapsulation stable NPs with a well-defined metal-silica and silica–environment (e.g., air) interface are obtained. Such encapsulation of NPs can be also exploited as an additional degree of freedom for tuning plasmon modes as both the size of the NPs[41] and the thickness of the silica shell[42,43] influence the excitation energy of the LSP modes. Moreover, by adjusting the thickness of the silica coating, a flexible adaption of the interparticle distance in assemblies is possible. Consequently, silica encapsulation represents a viable route for largely improving plasmonic properties of silver and other metallic NPs and their assemblies, greatly facilitating their use in plasmonic applications.[8]

In this study, we present an approach to effectively replace the CTAC-capping of Au@Ag NPs with a silica-shell of uniform and adaptable thickness, whereby the thickness of the silica shell can be controlled with high precision. Highly spatially resolved plasmon excitation maps obtained from Electron Energy-Loss Spectrum imaging in a Scanning Transmission Electron Microscope (STEM-EELS) demonstrate an excellent and highly reproducible optical response of the encapsulated NPs, which may be tuned through the shell thickness. Most notably, we reveal a strong enhancement of the plasmonic fields in the encapsulated NPs mediated through a coherent coupling of the surface plasmons of the Au@Ag NPs and the Mie resonances of the silica shell. We also demonstrate that this effect leads to an enhanced hybridization of coupled NPs which opens new possibilities for plasmonic applications.

2. Results and Discussion

The Au@Ag nanocubes (**Figure 1**a,b) are synthesized as previously published by Gómez-Graña et al.[36] and described Section 4. Au@Ag nanocubes with an edge length of (60 ± 1) nm are used for further modification. The growth of the silica layer is achieved by a modified procedure for gold NPs published by Montaño-Priede et al.[44] The overgrowth of the NPs with silica is conducted by a modified Stöber process[38] and requires a transfer of the Au@Ag NPs from aqueous solution to a solution of ammonia in ethanol (Figure 1c–f). The positive charge of the CTAC-capped NPs needs to be screened before the transfer to avoid their aggregation and flocculation.[40] This was achieved by washing and absorption of ω-thiol-terminated polyethylene glycol (PEG-SH) on the particle. Zeta potential measurements prove the change of the surface potential upon surfactant exchange (Figure S5, Supporting Information). The thickness of the silica shell can be tuned by varying the amount of tetraethyl orthosilicate (TEOS) added to the reaction solution which leads to a very precise control of surface plasmon energies in the following. Note, however, that the fabrication of silica shells with a thickness below a few nanometer, remains challenging. In order to systematically study the influence of the silica shell, Au@Ag NPs with an edge length of 60 nm and silica layers of 8, 12, 17, and 22 nm (see Figure 1) were characterized by spatially and spectrally highly-resolved STEM-EELS experiments (see Section 4 for details).

The EEL spectra of the cubic NPs exhibit five peaks corresponding to four different LSP modes and the silver bulk plasmon peak (**Figure 2**). The experimental spectra (Figure 2a) are in striking agreement (Figure 2b) with the simulated results (Figure 2c), which demonstrates the high quality of the silica shells and the dielectrically well-defined silver–silica interface. Here, the influence of the small gold nucleus in the Au@Ag NPs can be safely neglected due to the confinement of the LSPs to the silver–silica interface. Furthermore, the slightly increased broadening of all experimental peaks including the bulk plasmon is ascribed to imperfections of the silver structure of the NPs. In accordance with previous studies, the asymptotically converging red shift of the LSP modes increases with the silica shell thickness.[42,43] The latter opens pathways to finely tune the optical response of the NPs.

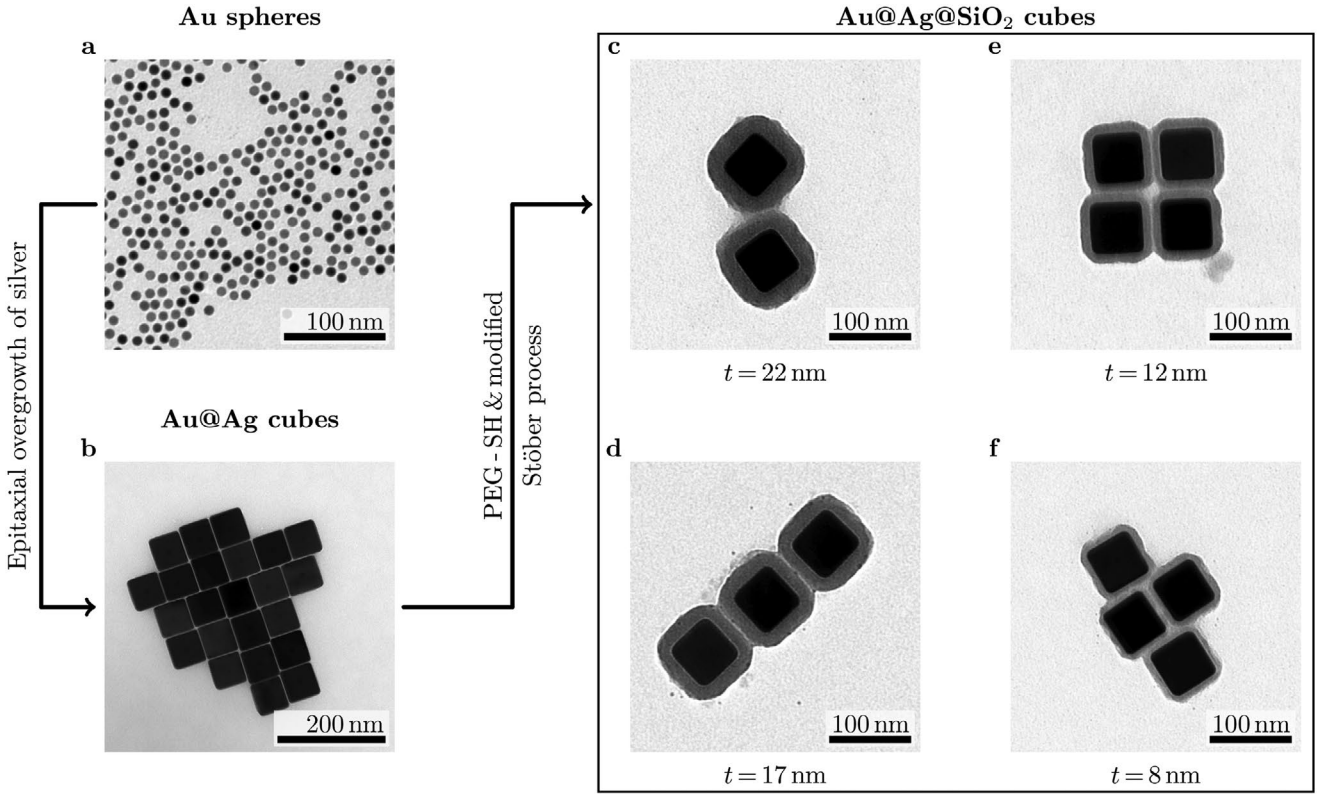

Figure 1. Schematic synthesis procedure for silica-encapsulated Au@Ag core–shell particles. a) First, gold spheres are synthesized that, b) second, are overgrown with silver. c–f) After functionalization with PEG-SH, they are encapsulated by a silica-shell using a modified Stöber process.

In order to classify the LSP modes, we employ a cubic harmonic basis derived from the angular momentum classification ($l = 1 \triangleq$ p, $l = 2 \triangleq$ d, $l = 3 \triangleq$ f, ⋯) of LSP eigenmodes in close agreement with atomic orbital categorization (see Section S4, Supporting Information). The LSP mode with highest excitation energy (3.65 eV at bare 60 nm Au@Ag nanocubes), denoted as fundamental mode in the following, corresponds to a superposition of energetically almost degenerated modes of high order in l. For small values of l the excitation energies of the LSP modes differ noticeable from the fundamental mode whereby

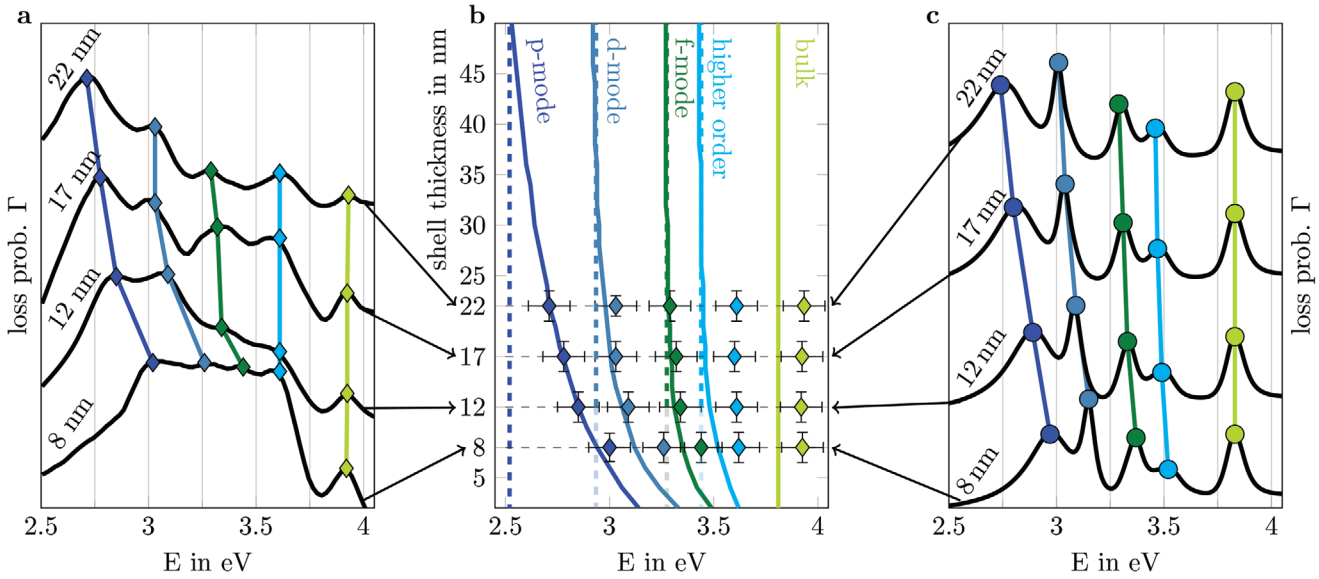

Figure 2. a) Experimental and c) simulated EEL spectra of 60 nm Au@Ag cubes with varying silica shell thickness. b) The comparison of experimental (diamonds) and simulated (solid line) LSP mode positions including mode character and asymptotic limits (dashed lines).

the energy splitting increases with decreasing value of *l*. In case of bare Au@Ag nanocubes, the p, d and f mode corresponding to 3.25, 3.45 and 3.6 eV, respectively, are clearly discernible from the fundamental mode at 3.65 eV (Figure 2). Accordingly, the LSP mode with the lowest excitation energy (p-mode) can be tuned in a range between 2.55 and 3.25 eV by increasing the silica shell thickness. On the other hand, the tunable range of the higher order LSP mode is very narrow (0.23 eV).

The observed red shift can be understood by describing the system with an adapted dielectric media approach. Here, the complex dielectric surrounding is described by an effective dielectric function obtained from a weighted average of silica and vacuum dielectric functions depending on the skin depth $d_s = |k^{-1}|$ of the plasmon wave that is exponential damped away from the interface ($\propto e^{-kz}$, where z is the distance from the interface and k is the plasmon wavevector). The logic behind this approach is as follows: when the thickness of the silica shell approaches zero, the effective dielectric function needs to match the dielectric function of vacuum. On the other hand, for the infinitely thick silica shell, the effective dielectric function should be equal to the dielectric function of silica. Between the two limits, the effective dielectric function follows a monotonous course, which is determined from the skin depth dependent weighting of the dielectric functions. For an infinite half-plane, the skin depth can be calculated analytically (see Section S5). For a silver–silica interface, the skin depth increases with decreasing excitation energy (see Figure S7b, Supporting Information). Therefore, the tunable range of excitation energy is larger for modes with lower excitation energy.

Similar to the resonance energy positions shown in Figure 2, the spatially resolved loss probability maps shown in **Figure 3**a excellently match the theoretical predictions. Minute spatial details of the SPR excitation are reproduced on length scales down to 5 nm. This again corroborates the high-quality of both the silica shell and the Au@Ag NP and their stability under both the electron beam and ambient conditions (see, e.g., ref. [5] for degraded optical properties of bare Au@Ag NPs).

Note furthermore that both the experimental and simulated spatially resolved surface plasmon maps reveal another intriguing feature of the thin silica shells, a strongly enhanced loss probability at the silica–vacuum interface compared to the bare Au@Ag NP reference in the range of 100% (see 1D cross section in Figure 3b,c. Considering that the loss probability is proportional to the *z*-component of the induced electric field of the LSP, this strong field enhancement directly increases the interaction of the silica-encapsulated NPs with their surroundings, for example, molecules attached to the shell (e.g., in sensing applications) or other NPs (e.g., in photonic crystals, see below). The effect arises from a resonant coupling between the surface plasmon modes located at the silica–silver interface and a broad Mie type resonance located at the vacuum–silica interface arising from a drop of the dielectric function from 2 to 1 in the considered energy range (see Section S6, Supporting Information).

To further corroborate the crucial field enhancement effect, we consider a simple coupling scenario, that is, the formation of hybridized plasmon modes in a dimer configuration (see **Figure 4**). It is well-known that the formation of split energy hybridized plasmon modes from (degenerated) single particle LSPs crucially depends on the coupling strength between the NPs. Accordingly, the coupling strength may be read-off from the energy splitting of the single particle modes. It quickly decays upon increasing interparticle distances beyond several nanometers in case of the bare 60 nm Au@Ag NPs, leading to a barely noticeable coupling effect if the interparticle distance exceeds 48 nm (see Section S7, Supporting Information). On the other hand, the field enhancement due to the silica shell strongly increases the interaction of the single particle modes (see Section S7, Supporting Information), leading to significantly stronger coupling effects (i.e., formation of distinct hybridized plasmon modes) up to 100 nm interparticle distance (50 nm silica shell). The hybridization leads to split energy levels of the LSP modes in the dimer EEL spectrum, for example, the modes indicated by i and ii in Figure 4a arising from hybridization of the single-particle *p*-mode (see Figure S7, Supporting

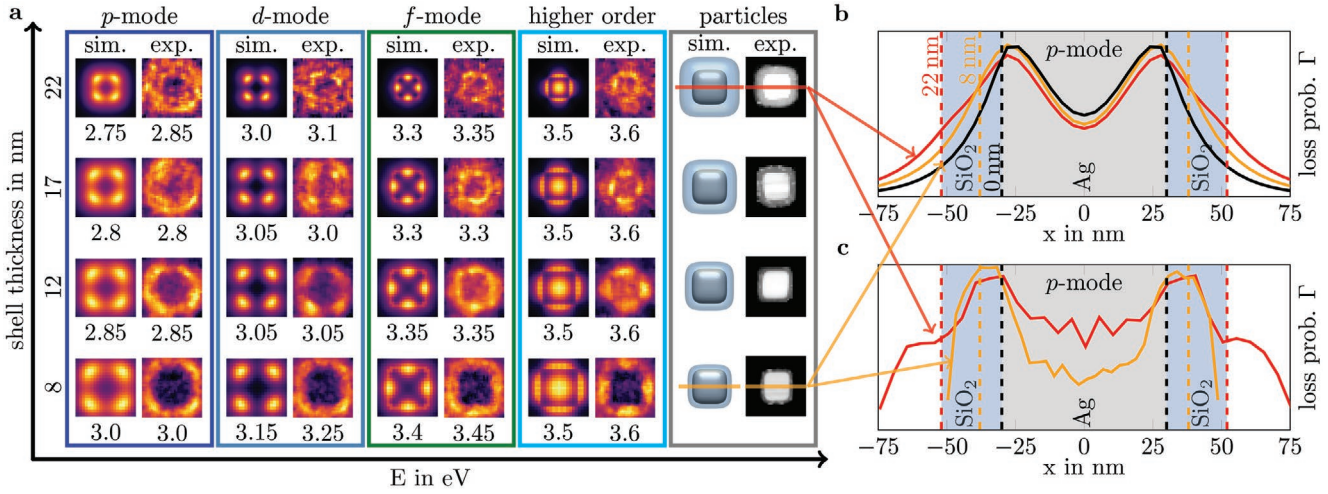

Figure 3. a) Simulated and experimental EEL probability maps in dependence of the silica shell thickness. b) Simulated and c) experimental loss probability line plots of the p-mode for 22 nm (red line) and 8 nm (orange line) silica shell thickness, respectively. Note the enhancement of the loss probability at the silica–vacuum interface (orange/red dashed lines respectively).

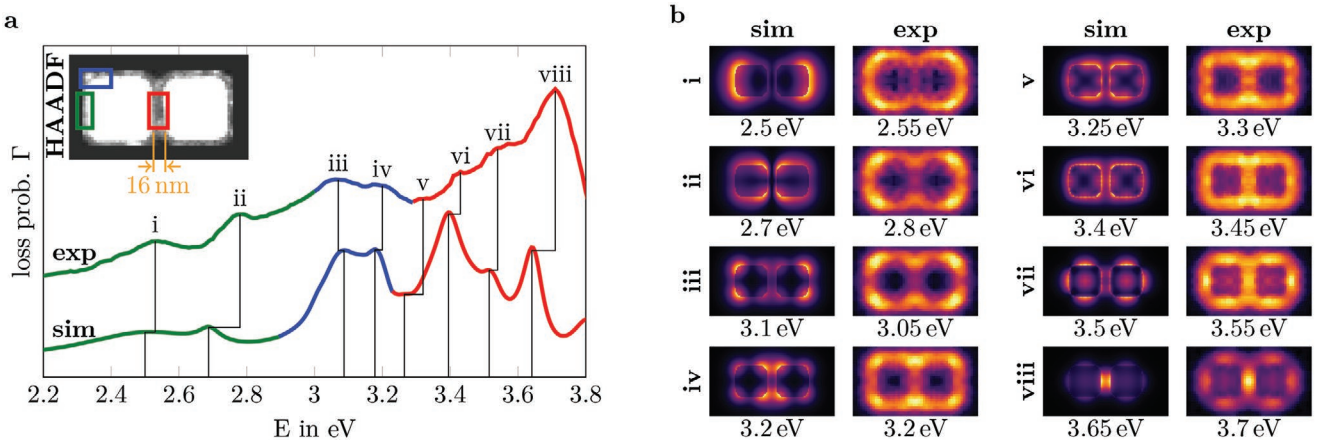

Figure 4. a) Experimental and simulated EEL spectra for a Au@Ag-cube dimer coated with 8 nm silica. Here, the color of the curve corresponds to different spatial sub-areas of the EELS scan, over which the loss probability is averaged. The different sub-areas are indicated by the red, blue, and green rectangles in the high angular dark field (HAADF) image of the dimer. b) EEL probability maps of the modes indicated (i–viii) in (a) respectively. The enhanced coupling of the LSP modes mediated by the silica coating results in a hybridization of the modes excitable in the single NPs, respectively. Note that the experimental obtained EEL probability maps are symmetrized with respect to the central plane of the dimer in order to enhance the signal to noise ratio.

Information, for a detailed explanation of the mode classification). The hybridized nature of the LSP modes is also visible through the spatially resolved loss maps plotted in Figure 4b. Both, the dimer EEL spectrum as well as the loss probability maps are again in striking agreement between experiment and simulation. We can conclude that the field enhancement is clearly expressed in the hybridized modes of the dimer.

3. Conclusion

In summary, we transferred the fabrication process of silica shell encapsulation from gold to Au@Ag NPs and thereby protected the silver surface. Employing high-resolution electron energy loss spectroscopy we demonstrate very well-defined dielectric response of the encapsulated Au@Ag NPs, not affected by environmental degradation (most notably oxidation). That includes reproduction of minute spatial details of the LSP excitation on length scales down to 5 nm. By modulating the silica shell thickness with nanometer precision single particle surface plasmon excitation energies could be tuned in a wide energy range between 2.55 and 3.25 eV. This behavior could be explained through an adapted dielectric media approach. Most notably, we discovered and explained a strong field enhancement at the vacuum–silica interface of the silica encapsulated Au@Ag NPs, originating from resonant coupling between LSPs at the silica–silver interface and a Mie type resonance at the vacuum–silica interface. We demonstrate the magnitude of the effect by creating strongly hybridized LSP modes in a NP dimer of 16 nm interparticle distance. Our findings open pathways toward fabrication of plasmonic oligomers, polymers, and colloidal crystals of well-defined geometry and structure (including interparticle distance), stability against environmental degradation, and strongly hybridized plasmon modes and bands over a large frequency range; and hence applications of the latter in sensing and signal transfer.

4. Experimental Section

Chemicals: Milli-Q water with a resistivity of 18.2 MΩ cm was used in all experiments. Chemicals were bought and used as received. Hexadecyltrimethylammonium bromide (CTAB, ≥99%), hydrogen tetrachloroaurate trihydrate ($HAuCl_4 \cdot 3\ H_2O$, ≥99.9%), cetyltrimethylammonium chloride solution (CTAC, 25 wt % in H_2O) and TEOS for synthesis were purchased from Sigma-Aldrich. Sodium borohydride ($NaBH_4$, ≥97%), L(+)-ascorbic acid (AA, ≥99%,), silver nitrate ($AgNO_3$, ≥99 %) and ethanol (EtOH, ≥99.5%, Ph. Eur., extra pure) were purchased from Roth. α-Methoxy-ω-mercapto polyethylene glycol (CH_3O-PEG-SH, M_w 5000 Dalton) was purchased from Rapp Polymere. Ammonia solution (NH_4OH, aq. 25%, for analysis) was purchased from Merck.

Characterization—UV–vis Characterization: UV–vis spectra were recorded using a Varian Cary 50 UV–vis spectrophotometer.

Zeta Potential Measurements: Zeta potential was measured on a Malvern Zetasizer Nano ZSP at 25° with 5·12 runs at a count rate of 197.8 kcps.

Analytical Ultracentrifugation (AUC) Measurements: The AUC measurements were performed on an Optima XL I (Beckman Coulter, Palo Alto, CA, United States) using Rayleigh interference optics and 12 mm double sector titanium centerpieces (Nanolytics, Potsdam, Germany). A SW 60 Ti Swinging-Bucket Rotor was used at 3000 RPM and 20°.

STEM EELS Characterization: To characterize the plasmonic response of the silica coated Au@Ag NPs STEM in combination with EELS[45–48] was applied in a probe Cs-corrected FEI Titan^3 transmission electron microscope (TEM). A focused electron-beam was scanned over the NPs with a dwell time of 30 ms. At each scanning point an EEL spectrum was recorded using a Gatan Tridiem energy filter. Simultaneously HAADF images under the convergence angle of 20 mrad and a collection angle of 7 mrad were acquired. The primary energy of 80 keV of the beam electrons was monochromized to ±40 meV using the Wien filter of the TEM. To avoid contamination, the samples were plasma-cleaned for 8 s in advance. Using this technique, the position of the characteristic peaks in the EEL spectra corresponding to LSP modes excited by the beam electrons were studied for NPs with different silica shell thickness. Furthermore, the spatial distribution of the induced plasmonic fields were studied by extracting spatially resolved EEL probability maps of the different LSP modes. To correct for the scattering absorption, the spatial resolved EELS signal was normalized by the overall intensity at the corresponding scanning position respectively $(\Gamma_{norm}(x, y, \omega) = \Gamma(x, y, \omega)/\int\Gamma(x, y, \omega)\mathrm{d}\omega)$.

Synthesis of Nanoparticles—Synthesis of Initial Gold Seeds: An aqueous solution of $HAuCl_4$ (0.25 mL, 0.01 M) and an aqueous solution of CTAB (7.50 mL, 0.10 M) were mixed in a glass vial (50 mL) and tempered to 27°. Freshly prepared, ice-cold $NaBH_4$ solution (0.60 mL of 0.01 M) was added under vigorous stirring. The seed solution was aged for 90 min at 27° to ensure complete decomposition of excess borohydride.

Synthesis of Spherical Gold Seeds: Spherical gold seeds with a diameter of 9.5 nm were synthesized as previously described.[31,34] In a typical synthesis, an aqueous solution containing CTAC (39.00 mL, 0.10 M) and $HAuCl_4$ (1.00 mL, 0.01 M) was tempered to 27° in a water bath. AA (15.00 mL, 0.10 M) was added, followed by a rapid injection of 500 µL initial seeds. The solution was kept at 27° for 15 min. The spherical seeds were characterized by UV–vis spectroscopy, TEM and AUC. The polydispersity index (PDI) of the samples was 1.04 (Figures S1 and S2 and Equation (S1), Supporting Information).

Synthesis of Au@Ag Cubes: Au@Ag cubes were synthesized by a procedure published by Gómez-Graña et al.[36] Typically, water (21.00 mL), CTAC (3.00 mL, 0.10 M), AA (1.20 mL, 0.10 M) and 275 µL of as prepared spherical seeds were mixed. Then, $AgNO_3$ (3.00 mL, 0.01 M) was added and the solution was heated to 65° and left undisturbed for 12 h.[36] The particles were collected by centrifugation (5000 RPM, 5 min). The Au@Ag cubes were characterized by TEM and UV–vis spectroscopy (Figure S3, Supporting Information). The yield of cubic Au@Ag particles was 85% (Figure S4, Supporting Information).

Synthesis of Au@Ag@SiO_2 Cubes: The synthesis was adapted from previously published procedure for the silica coating of gold NPs by Montaño-Priede et al.[44] 60 mL of the synthesized Au@Ag cubes were centrifuged at 9000 RPM for 4 min. The supernatant was removed, and the particles were redispersed in CTAC (28.00 mL, 0.05 M). The dispersion was centrifuged at 6000 RPM for 10 min. The supernatant was removed, and the particles were redispersed in 5 mL MilliQ containing 0.79 mg PEG-SH, afterward CTAC (5.00 mL, 0.05 M) was added. The solution was left undisturbed for 1 h. The particles were concentrated to 1.35 mL at 6000 RPM for 10 min. Two further solutions were prepared. For the first solution (solution 1), 1 mL NH_4OH was added to 37.5 mL of EtOH. For the second solution (solution 2), 50 µL TEOS were added to 7.4 mL of EtOH. The concentrated NP solution (1.35 mL) was added to 2.5 mL EtOH and 3.85 mL of solution 1. Then, varying volumes of solution 2 were added (Table S1, Supporting Information). The reaction mixture was stored at 30° for 2 h. For the preparation of TEM samples 750 µL of the dispersion and 150 µL of 5 mM CTAC were centrifuged at 6500 RPM for 5 min and redispersed in 1 mM CTAC solution. Zeta potential measurements of particles capped with CTAC and PEG-SH are depicted in Figure S5, Supporting Information.

Electromagnetic Simulations: The plasmonic response of the NPs was simulated using a Boundary Element Method (MNPBEM code) implemented by Hohenester et al.[49,50] Applying the MNPBEM code the plasmonic response was calculated by solving the full Maxwell equations for 80 keV electrons exciting plasmon modes in silica coated silver cubes with 60 nm edge length. The dielectric functions of silver and silica are taken from refs. [51] and [52]. The medium surrounding the NPs was assumed to be vacuum ($\varepsilon = 1$). The influence of the small gold nucleus in the Au@Ag NPs can be safely neglected in the simulation due to the confinement of the plasmons to the silver–silica interface.

Supporting Information

Supporting Information is available from the Wiley Online Library or from the author.

Acknowledgements

J.S. and F.K. contributed equally to this work. A.L. has received funding from the European Research Council (ERC) under the Horizon 2020 research and innovation program of the European Union (grant agreement no. 715620). J.S. received funding from the Deutsche Forschungsgemeinschaft (DFG, German Research Foundation) under Germany's Excellence Strategy through Würzburg-Dresden Cluster of Excellence on Complexity and Topology in Quantum Matter—ct.qmat (EXC 2147, project-id 390858490). F.K and E.S. acknowledge Deutsche Forschungsgemeinschaft (DFG, German Research Foundation) under SFB 1214, project B1 and Zukunftskolleg at the University of Konstanz for financial support. P.P. received funding from the Deutsche Forschungsgemeinschaft (project-id 431448015). The authors thank Rose Rosenberg for AUC measurements and data evaluation.

Open access funding enabled and organized by Projekt DEAL.

Conflict of Interest

The authors declare no conflict of interest.

Data Availability Statement

Research data are not shared.

Keywords

core–shell particles, electron energy-loss spectrum, nanoparticles, plasmonics, silica, surface plasmon resonance

Received: June 16, 2021
Revised: August 17, 2021
Published online: September 23, 2021

[1] J. N. Anker, W. P. Hall, O. Lyandres, N. C. Shah, J. Zhao, R. P. Van Duyne, *Nat. Mater.* **2008**, *7*, 442.
[2] R. X. He, R. Liang, P. Peng, Y. Norman Zhou, *J. Nanopart. Res.* **2017**, *19*, 267.
[3] B. Goris, G. Guzzinati, C. Fernández-López, J. Pérez-Juste, L. M. Liz-Marzán, A. Trügler, U. Hohenester, J. Verbeeck, S. Bals, G. Van Tendeloo, *J. Phys. Chem. C* **2014**, *118*, 15356.
[4] L. García-Cruz, V. Montiel, J. Solla-Gullón, *3 Shape-Controlled Metal Nanoparticles for Electrocatalytic Applications, Vol. 1A: Metallic Nanomaterials* (Ed: C. Kumar), De Gruyter, Berlin, Boston **2019**, pp. 103–156.
[5] D. Schletz, J. Schultz, P. L. Potapov, A. M. Steiner, J. Krehl, T. A. F. König, M. Mayer, A. Lubk, A. Fery, *Adv. Opt. Mater.* **2021**, *9*, 2001983.
[6] J. Crespo, A. Falqui, J. García-Barrasa, J. M. López-De-Luzuriaga, M. Monge, M. E. Olmos, M. Rodríguez-Castillo, M. Sestu, K. Soulantica, *J. Mater. Chem. C* **2014**, *2*, 2975.
[7] C. Burda, X. Chen, R. Narayanan, M. A. El-Sayed, *Chem. Rev.* **2005**, *105*, 1025.
[8] C. Hanske, M. N. Sanz-Ortiz, L. M. Liz-Marzán, *Adv. Mater.* **2018**, *30*, e1707003.
[9] K. C. Vernon, A. M. Funston, C. Novo, D. E. Gómez, P. Mulvaney, T. J. Davis, *Nano Lett.* **2010**, *10*, 2080.
[10] H. Chen, F. Wang, K. Li, K. C. Woo, J. Wang, Q. Li, L. D. Sun, X. Zhang, H. Q. Lin, C. H. Yan, *ACS Nano* **2012**, *6*, 7162.
[11] E. Prodan, C. Radloff, N. J. Halas, P. Nordlander, *Science* **2003**, *302*, 419.
[12] M. Mayer, P. L. Potapov, D. Pohl, A. M. Steiner, J. Schultz, B. Rellinghaus, A. Lubk, T. A. Konig, A. Fery, *Nano Lett.* **2019**, *19*, 3854.
[13] P. Nordlander, C. Oubre, E. Prodan, K. Li, M. I. Stockman, *Nano Lett.* **2004**, *4*, 899.

[14] J. M. McMahon, S. K. Gray, G. C. Schatz, *Phys. Rev. B* **2011**, *83*, 115428.
[15] N. J. Halas, S. Lal, W. S. Chang, S. Link, P. Nordlander, *Chem. Rev.* **2011**, *111*, 3913.
[16] P. K. Jain, W. Huang, M. A. El-Sayed, *Nano Lett.* **2007**, *7*, 2080.
[17] N. Hooshmand, M. A. El-Sayed, *Proc. Natl. Acad. Sci. USA* **2019**, *116*, 19299.
[18] W. Zhu, M. G. Banaee, D. Wang, Y. Chu, K. B. Crozier, *Small* **2011**, *7*, 1761.
[19] E. Menumerov, S. D. Golze, R. A. Hughes, S. Neretina, *Nanoscale* **2018**, *10*, 18186.
[20] L. Sun, H. Lin, K. L. Kohlstedt, G. C. Schatz, C. A. Mirkin, *Proc. Natl. Acad. Sci. USA* **2018**, *115*, 7242.
[21] B. Gao, G. Arya, A. R. Tao, *Nat. Nanotechnol.* **2012**, *7*, 433.
[22] E.-M. Roller, L. V. Besteiro, C. Pupp, L. K. Khorashad, A. O. Govorov, T. Liedl, *Nat. Phys.* **2017**, *13*, 761.
[23] Y. Zhao, C. Xu, *Adv. Mater.* **2020**, *32*, 1907880.
[24] L. Bahrig, S. G. Hickey, A. Eychmüller, *CrystEngComm.* **2014**, *16*, 9408.
[25] J. Brunner, B., R. Rosenberg, S. Sturm, H. Cölfen, E. V. Sturm, *Chem. - Eur. J.* **2020**, *26*, 15242.
[26] M. Kapuscinski, P. Munier, M. Segad, L. Bergström, *Nano Lett.* **2020**, *20*, 7359.
[27] E. V. Sturm (née Rosseeva), H. Cölfen, *Chem. Soc. Rev.* **2016**, *45*, 5821.
[28] N. R. Jana, L. Gearheart, C. J. Murphy, *Adv. Mater.* **2001**, *13*, 1389.
[29] W. Niu, L. Zhang, G. Xu, *Nanoscale* **2013**, *5*, 3172.
[30] H. Heinz, C. Pramanik, O. Heinz, Y. Ding, R. K. Mishra, D. Marchon, R. J. Flatt, I. Estrela-Lopis, J. Llop, S. Moya, R. F. Ziolo, *Surf. Sci. Rep.* **2017**, *72*, 1.
[31] F. Kirner, P. Potapov, J. Schultz, J. Geppert, M. Müller, G. González-Rubio, S. Sturm, A. Lubk, E. Sturm, *J. Mater. Chem. C* **2020**, *8*, 10844.
[32] M. Grzelczak, J. Pérez-Juste, P. Mulvaney, L. M. Liz-Marzán, *Chem. Soc. Rev.* **2008**, *37*, 1783.
[33] M. A. Boles, M. Engel, D. V. Talapin, *Chem. Rev.* **2016**, *116*, 11220.
[34] Y. Zheng, Y. Ma, J. Zeng, X. Zhong, M. Jin, Z. Y. Li, Y. Xia, *Chem. - Asian J.* **2013**, *8*, 792.
[35] S.-J. Jeon, J.-H. Lee, E. L. Thomas, *J. Colloid Interface Sci.* **2014**, *435*, 105.
[36] S. Gómez-Graña, B. Goris, T. Altantzis, C. Fernández-López, E. Carbó-Argibay, A. Guerrero-Martínez, N. Almora-Barrios, N. López, I. Pastoriza-Santos, J. Pérez-Juste, S. Bals, G. Van Tendeloo, L. M. Liz-Marzán, *J. Phys. Chem. Lett.* **2013**, *4*, 2209.
[37] G. A. Sotiriou, T. Sannomiya, A. Teleki, F. Krumeich, J. Vörös, S. E. Pratsinis, *Adv. Funct. Mater.* **2010**, *20*, 4250.
[38] W. Stöber, A. Fink, E. Bohn, *J. Colloid Interface Sci.* **1968**, *26*, 62.
[39] Y. Kobayashi, H. Katakami, E. Mine, D. Nagao, M. Konno, L. M. Liz-Marzán, *J. Colloid Interface Sci.* **2005**, *283*, 392.
[40] I. Pastoriza-Santos, J. Pérez-Juste, L. M. Liz-Marzán, *Chem. Mater.* **2006**, *18*, 2465.
[41] L. Hung, S. Y. Lee, O. McGovern, O. Rabin, I. Mayergoyz, *Phys. Rev. B* **2013**, *88*, 75424.
[42] J. Rodríguez-Fernández, I. Pastoriza-Santos, J. Pérez-Juste, F. J. García De Abajo, L. M. Liz-Marzán, *J. Phys. Chem. C* **2007**, *111*, 13361.
[43] K. Kluczyk-Korch, C. David, W. Jacak, J. Jacak, *Materials.* **2019**, *12*, 3192.
[44] J. L. Montaño-Priede, J. P. Coelho, A. Guerrero-Martínez, O. Peña-Rodríguez, U. Pal, *J. Phys. Chem. C* **2017**, *121*, 9543.
[45] J. Nelayah, M. Kociak, O. Stéphan, F. J. G. De Abajo, M. Tencé, L. Henrard, D. Taverna, I. Pastoriza-Santos, L. M. Liz-Marzán, C. Colliex, *Nat. Phys.* **2007**, *3*, 348.
[46] F.-P. Schmidt, H. Ditlbacher, U. Hohenester, A. Hohenau, F. Hofer, J. R. Krenn, *Nano Lett.* **2012**, *12*, 5780.
[47] J. Martin, M. Kociak, Z. Mahfoud, J. Proust, D. Gérard, J. Plain, *Nano Lett.* **2014**, *14*, 5517.
[48] D. Yoshimoto, H. Saito, S. Hata, Y. Fujiyoshi, H. Kurata, *ACS Photonics* **2018**, *5*, 4476.
[49] U. Hohenester, A. Trügler, *Comput. Phys. Commun.* **2012**, *183*, 370.
[50] U. Hohenester, *Comput. Phys. Commun.* **2014**, *185*, 1177.
[51] H. U. Yang, J. D'Archangel, M. L. Sundheimer, E. Tucker, G. D. Boreman, M. B. Raschke, *Phys. Rev. B* **2015**, *91*, 235137.
[52] L. Gao, F. Lemarchand, M. Lequime, *Opt. Express* **2012**, *20*, 15734.